Gain-phase modulation in chirped-pulse amplification

Yijie Shen, Gan Gao, Yuan Meng, Xing Fu, and Mali Gong*
State Key Laboratory of Precision Measurement Technology and Instruments, Center for Photonics and Electronics, Department of Precision Instruments, Tsinghua University, Beijing 100084, China
(Received 2 May 2017; published 23 October 2017)

The cross-modulation between the gain and chirped phase in chirped-pulse amplification (CPA) is theoretically and experimentally demonstrated. We propose a gain-phase coupled nonlinear Schrödinger equation (GPC-NLSE) for solving chirped-pulse propagation in a nonlinear gain medium involved in the gain-phase modulation (GPM) process. With the GPC-NLSE, the space-time-frequency-dependent gain, chirped phase, pulse, and spectrum evolutions can be precisely calculated. Moreover, a short-length high-gain Yb-doped fiber CPA experiment is presented in which a self-steepening distortion of the seed pulse is automatically compensated after amplification. This phenomenon can be explained by the GPM theory whereas conventional models cannot. The experimental results for the temporal and spectral intensities show excellent agreement with our theory. Our GPM theory paves the way for further investigations of the finer structures of the pulse and spectrum in CPA systems.

DOI: 10.1103/PhysRevA.96.043851

I. INTRODUCTION

The nonlinear Schrödinger equation (NLSE) is widely used in solving the evolution of an optical chirped pulse in nonlinear medium, which has successfully explained various physical phenomena such as optical solitons, self-steepening, and pulse splitting [1–4]. Recently, the NLSE has been modified to describe many new physical effects such as two-photon absorption and free-carrier temporal effects in silicon waveguides and photonic nanowires [5–7]. It is a key problem to consider gain dispersion and gain saturation effects in NLSE models. For the gain dispersion, the gain effect can be interpreted as a spectral modulator with a Gaussian or parabolic function in the NLSE [8–11], which has been combined with stimulated Raman scattering [8], four-wave mixing [10], and dissipative soliton formation [11]. For the transient gain, the gain saturation model was applied to modify the NLSE with a parameter of saturation power or energy, which explained the mode-locking process [12] and self-similar pulse evolution [13] in all-normal-dispersion lasers. Recently, a new gain saturation model was reported [14] but it has not combined the NLSE with detailed physical processes. For the combined effects of gain bandwidth and gain saturation, some complex coupled types of NLSE have been proposed for the application of various ultrafast laser systems [15–17].

However, three problems remain to be further investigated: (1) The gain spectrum cannot be simply written as a certain function when considering the complex processes underlying the population and energy-level dynamics in a gain medium. (2) The gain saturation model is derived under the steady-state assumption. Nevertheless, the duration of an ultrashort pulse is always much shorter than the response time of the gain medium, where the gain saturation model may fail [18]. Although some typical values of saturation power or energy were valid in several special conditions [15–17], the general principle remains unavailable. (3) The gain can induce chirped phase changes and the instantaneous frequency can influence transient gain redistribution. This complex gain-phase modulation (GPM) effect is neglected in most conventional NLSE models. The physical principles of the gain-coupling effects have been studied [19] but it cannot be ascribed to the NLSE. The conventional NLSE model is summarized in Appendix A.

The above problems are vital to chirped-pulse amplification (CPA) systems, in which the pulse shape always requires optimization through spectral shaping [20,21] and suppressing gain narrowing [22,23]. For gain dispersion, the Frantz-Nodvik formula [24–26] and inhomogeneous broadening model [27] were always used to investigate pulse evolution, while they exclude the time-dependent gain caused by changes in transient power. The coupled rate equations with different frequency components can further characterize the time-frequency-dependent gain more precisely [28], yet they cannot reveal the influences of chirps. A multiwavelength mode-locking model can solve the chirp phase and instantaneous frequency [29] but neglects the interaction between the gain and chirp.

In this paper, we establish a theoretical model to investigate the interaction between gain and chirped phase. The NLSE coupled with rate equations is modified to solve the pulse and spectrum evolutions during CPA. Our model can precisely solve the space-time-dependent gain, chirped phase, pulse, and spectrum evolutions. We also conducted a high-gain ytterbium-doped fiber (YDF) CPA system. The aberrant and self-steepening seed pulse was measured, but, after CPA, the distortion was alleviated. This phenomenon is successfully explained by our GPM theory. The pulse evolution process during CPA has been successfully simulated and the theoretical results show excellent agreement with experimental results.

II. THEORETICAL MODEL

A. Gain spectrum dynamics

In the YDF amplifier, the laser and population dynamics are described by the rate equations [30–33]

$$\frac{1}{c_s}\frac{\partial P_s^{\pm}}{\partial t} \pm \frac{\partial P_s^{\pm}}{\partial z} = \left[\Gamma_s\left(\sigma_{em}^{(s)}N_2 - \sigma_{ab}^{(s)}N_1\right) - \alpha_s\right]P_s^{\pm}, \quad (1)$$

*gongml@mail.tsinghua.edu.cn

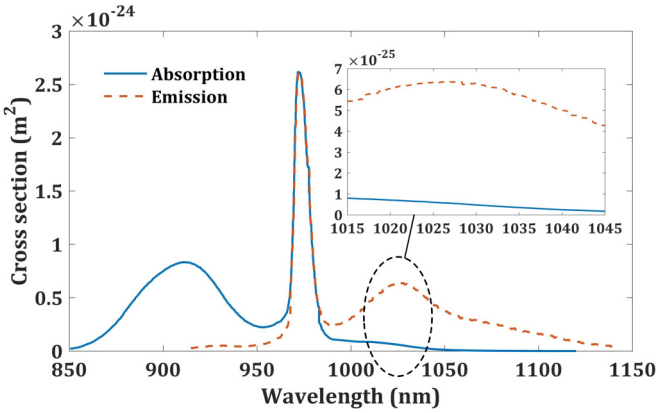

FIG. 1. The absorption and emission cross sections versus wavelength in YDF.

$$\frac{1}{c_p}\frac{\partial P_p^{\pm}}{\partial t} \pm \frac{\partial P_p^{\pm}}{\partial z} = \left[\Gamma_p\left(\sigma_{em}^{(p)}N_2 - \sigma_{ab}^{(p)}N_1\right) - \alpha_p\right]P_p^{\pm}, \quad (2)$$

$$\frac{\partial N_2}{\partial t} = \left(\sigma_{ab}^{(s)}N_1 - \sigma_{em}^{(s)}N_2\right)\frac{\Gamma_s(P_s^+ + P_s^-)}{A_c hc/\lambda_s} - \frac{N_2}{\tau} + \left(\sigma_{ab}^{(p)}N_1 - \sigma_{em}^{(p)}N_2\right)\frac{\Gamma_p(P_p^+ + P_p^-)}{A_c hc/\lambda_p}, \quad (3)$$

where the superscript "+ (−)" corresponds to the forward (backward) propagating direction, the subscript "s (p)" corresponds to laser (pump) light, N_1 (N_2) is the population density of the lower (upper) energy-level manifold, $N_{tot} = N_1 + N_2$ is the total ion-doping concentration, $\sigma_{ab}^{(*)}$ ($\sigma_{em}^{(*)}$) is the effective absorption (emission) cross section, Γ is the filling factor of the fiber core, α is the intrinsic scattering loss in the fiber, h is Planck's constant, c is the speed of light, τ is the upper-state lifetime, $A_c = \pi a_c^2/4$ is the cross-sectional area of the fiber core, and a_c is the fiber core diameter.

The initial powers of the pump light and seed laser, $P_p(t)|_{z=0}$ and $P_s(t)|_{z=0}$, are known as the initial conditions of the rate equations. The population densities of the lower and upper energy levels, $N_1(t)$ and $N_2(t)$, can then be solved. Because the pump and laser light are both quasimonochromatic, the effective cross sections are valid in solving the rate equations, as shown in Appendix C. However, the actual gain also varies with light frequency, which is determined by the frequency-dependent absorption and emission cross sections, $\sigma_{ab}(\omega)$ and $\sigma_{em}(\omega)$, as Fig. 1 shows. Thus, in our model, the frequency-time-dependent gain is written as

$$g(\omega,t) = \Gamma_s[\sigma_{em}(\omega)N_2(t) - \sigma_{ab}(\omega)N_1(t)] - \alpha_s, \quad (4)$$

which is useful in modeling the evolutions of pulse and spectrum shapes in the following sections.

B. Gain-phase modulation

The light field of a chirped pulse is written as $E(t) = A(t)e^{i\omega_0 t}$, where the complex envelope $A(t) = \sqrt{P_s(t)}e^{i\phi(t)}$, $\phi(t)$ is the temporal phase, and ω_0 is the center frequency of the laser. The spectrum field is expressed as $\widetilde{E}(\omega) = \sqrt{I_s(\omega)}e^{i\varphi(\omega)}$, where $\varphi(\omega)$ is the spectral phase and the laser power is related to the light field as $P_s = |E(t)|^2$. Similarly, the laser spectrum intensity is related to the spectrum field as $I_s = |\widetilde{E}(\omega)|^2$. The light and spectrum fields satisfy the Fourier transform relation, obeying the wave equation and its form in the Fourier frequency domain [34]:

$$\nabla^2\mathbf{E} - \frac{1}{c^2}\frac{\partial^2\mathbf{E}}{\partial t^2} = \mu_0\frac{\partial^2\mathbf{P}_L(\mathbf{E})}{\partial t^2} + \mu_0\frac{\partial^2\mathbf{P}_{NL}(\mathbf{E})}{\partial t^2}, \quad (5)$$

$$\nabla^2\widetilde{\mathbf{E}} + \varepsilon_r(\omega)k^2\widetilde{\mathbf{E}} = 0, \quad (6)$$

where $k = \omega/c = 2\pi/\lambda$, $c = 1/\sqrt{\mu_0\varepsilon_0}$, μ_0 is the vacuum permeability, ε_0 is the vacuum permittivity, $\mathbf{P}_L$ ($\mathbf{P}_{NL}$) is the linear (nonlinear) polarization, $\varepsilon_r = n^2$ is the relative permittivity, and n is the refractive index. A chirped laser pulse propagating along the z axis is expressed as $E(z+\Delta z) = E(z)e^{-ikn\Delta z}$, satisfying the following assumptions [34]: (1) The optical field is assumed to be quasimonochromatic, i.e., $\Delta\omega/\omega_0 \ll 1$, where $\Delta\omega$ is the spectral width. (2) The slowly varying envelope approximation: the duration of the pulse envelope is much larger than an optical cycle. (3) $\mathbf{P}_{NL}$ is treated as a small perturbation to $\mathbf{P}_L$ since the nonlinear changes in the refractive index are less than 10^{-6}. Thus, the gain and nonlinear effects can be ascribed to the small variation of complex refractive index: $\varepsilon_r = n^2 = (n_0 + \Delta n)^2 \approx n_0^2 + 2n_0\Delta n$, $\Delta n = \Delta n_G + \Delta n_{NL}$, and then the equation for the envelope function in the retarded frame becomes

$$\frac{\partial A}{\partial z} = -\frac{i\beta_2}{2}\frac{\partial^2 A}{\partial T^2} + \frac{\beta_3}{6}\frac{\partial^3 A}{\partial T^3} + ik\Delta n A, \quad (7)$$

where $T = t - \beta_1 z$ is the retarded time, β_1 is the first-order dispersion, β_2 is the group velocity dispersion (GVD), β_3 is the third-order dispersion (TOD), n_0 is the intrinsic mode refractive index, Δn is the perturbance of the refractive index, Δn_G (Δn_{NL}) is change in the gain-induced (nonlinear) refractive index, while the dispersions of orders higher than 3 are neglected. Considering the Kerr effect, the nonlinear refractive index is given by $\Delta n_{NL} = n_2|A|^2/A_{eff}$, where n_2 is the Kerr refractive index coefficient and A_{eff} is the effective core area. According to the definition of gain, the gain-induced refractive index is given by $\Delta n_G = -ig/(2k)$. Hereinafter, we focus on the gain-phase cross-modulating relationship and its influences on chirped-pulse evolution. The gain is related to both the frequency-dependent cross sections $\sigma_{ab}(\omega)$, $\sigma_{em}(\omega)$ in the frequency domain and the population dynamics $N_1(T)$, $N_2(T)$ in the time domain. The method of variable separation is used to express the binary gain relation [28]: $g(\omega,T) = g_t g_\omega/g_0$, where $g_t = g(T)|_{\omega=\omega_0}$, $g_\omega = g(\omega)|_{T=T_0}$, $g_0 = g(\omega_0,T_0)$, and $\omega_0 = 2\pi c/\lambda_s$. For a stable laser pulse sequence, T_0 satisfies the moment when the population is equal to the corresponding mean value, $N_1(T_0) = \bar{N}_1(T)$, $N_2(T_0) = \bar{N}_2(T)$. In the frequency domain, g_ω modulates the spectrum field. While in the time domain, the time-varying phase $\phi(t)$ implies that the instantaneous optical frequency $\omega_{ins}(t)$ differs across the pulse from its central value ω_0 with $\delta\omega = \partial\phi/\partial t$. The phase and gain are interactional and both involved in Eq. (7). According to the above principles, the gain-phase coupled nonlinear Schrödinger equation (GPC-NLSE)

is established to characterize the GPM process as follows:

$$g_t = \Gamma_s[\sigma_{em}(\omega_{ins})N_2(T) - \sigma_{ab}(\omega_{ins})N_1(T)] - \alpha_s, \quad (8)$$

$$g_\omega = \Gamma_s[\sigma_{em}(\omega)N_2(T_0) - \sigma_{ab}(\omega)N_1(T_0)] - \alpha_s, \quad (9)$$

$$\frac{\partial A}{\partial z} = -\frac{i\beta_2}{2}\frac{\partial^2 A}{\partial T^2} + \frac{\beta_3}{6}\frac{\partial^3 A}{\partial T^3} + i\gamma|A|^2 A + \frac{g_t g_\omega}{2g_0}A, \quad (10)$$

where $\gamma = \omega_0 n_2/(cA_{eff})$. The temporal gain g_t distribution induced by the time-dependent instantaneous frequency $\omega_{ins}(T) = \omega_0 + \frac{\partial\phi(z,T)}{\partial T}$ is considered. The separation of g_t and g_ω also lays the foundation for the corresponding numerical methods in the following section. The separation is valid as the quasimonochromatic assumption is used. This assumption is valid for ~1-μm wavelength pulses with the spectral width of dozens of nanometers. If the assumption fails, the accuracy of the separation may decrease.

C. Numerical methods

The NLSE is a nonlinear partial differential equation that does not generally lend itself to analytic solutions in general. As an effective numerical method, the split-step Fourier method (SSFM) is therefore widely used to solve the NLSE [34,35]. In analogy with the conventional NLSE, the GPC-NLSE can also be formally written in operator form:

$$\frac{\partial A(z,T)}{\partial z} = [\widehat{D}(\omega) + \widehat{N}(T) + \widehat{G}(\omega,T)]A(z,T), \quad (11)$$

$$\widehat{D}(\omega) = i\left(\frac{\beta_2}{2}\widetilde{\omega}^2 + \frac{\beta_3}{6}\widetilde{\omega}^3\right), \quad (12)$$

$$\widehat{N}(T) = i\gamma|A(z,T)|^2, \quad (13)$$

$$\widehat{G}(\omega,T) = \frac{g_t(T)g_\omega(\omega)}{2g_0}, \quad (14)$$

where $\widetilde{\omega} = \omega - \omega_0$, $\widehat{D}$, $\widehat{N}$, and $\widehat{G}$ are respectively the dispersion, nonlinear, and gain operators. The conventional SSFM can be applied when regarding the gain term as constant or purely a frequency-dependent term (gain bandwidth narrowing models) or purely a time-dependent term (gain saturation models), but is unable to deal with the frequency-time-dependent gain operator. We present below a modification of the numerical method to deal with the GPC-NLSE. An approximate solution of Eq. (11) is obtained by assuming the propagation of the optical field over a small distance Δz. Mathematically,

$$\begin{aligned} A(z+\Delta z,T) &= \exp\langle\Delta z(\widehat{D}+\widehat{N}+\widehat{G})\rangle A(z,T) \\ &\approx \exp\langle\Delta z\widehat{D}\rangle \exp\langle\Delta z\widehat{N}\rangle \exp\langle\Delta z\widehat{G}\rangle A(z,T). \end{aligned} \quad (15)$$

The higher-order error induced by the noncommutability among operators, $\exp\langle\Delta z\widehat{D}\rangle$, $\exp\langle\Delta z\widehat{N}\rangle$, $\exp\langle\Delta z\widehat{G}\rangle$, can be evaluated by the Baker-Hausdorff formula [34,36], where the exponential operator for a certain operator $\exp\langle\widehat{X}\rangle$ to an arbitrary (z,T)-dependent function $B(z,T)$ is defined in the Fourier domain using the prescription $\exp\langle\widehat{X}\rangle B(z,T) = \mathcal{F}^{-1}\{\exp(\widehat{X})\mathcal{F}[B(z,T)]\}$, which can be directly calculated by the finite Fourier transform (FFT) algorithm. Specially, if operator $\widehat{X}$ is only time dependent, the exponential operator would be equivalent to a simple exponent function $\exp\langle\widehat{X}\rangle = \exp(\widehat{X})$. As the dispersion operator and nonlinear operator can both be determined, the expression for the gain operator can be derived as

$$\begin{aligned} \exp\langle\Delta z\widehat{G}(\omega,T)\rangle B(z,T) &= \mathcal{F}^{-1}\left\{\exp\left[\frac{\Delta z}{2g_0}g_\omega(\omega)g_t(T)\right]\mathcal{F}[B(z,T)]\right\} \\ &\approx \mathcal{F}^{-1}\left\{\left[1 + \frac{\Delta z}{2g_0}g_\omega(\omega)g_t(T) + \frac{1}{2}\frac{\Delta z^2}{4g_0^2}g_\omega^2(\omega)g_t^2(T) + \cdots\right]\mathcal{F}[B(z,T)]\right\} \\ &= B(z,T) + \frac{\Delta z}{2g_0}g_t(T)\mathcal{F}^{-1}\{g_\omega(\omega)\mathcal{F}[B(z,T)]\} + \frac{\Delta z^2}{8g_0^2}g_t^2(T)\mathcal{F}^{-1}\left\{g_\omega^2(\omega)\mathcal{F}[B(z,T)]\right\} + \cdots. \end{aligned} \quad (16)$$

Hence, the main difficulty is in treating the term $\exp[\frac{\Delta z}{2g_0}g_\omega(\widetilde{\omega})g_t(T)]$ so that it can operate in the time domain or Fourier domain. Therefore, we use the Taylor expansion of exponential function, $e^x \approx 1 + \frac{1}{1!}x + \frac{1}{2!}x^2 + \cdots$, and higher-order terms are neglected here because the error can be confined to acceptable tolerances under a suitable step Δz. To reduce the error induced by the noncommutability among operators, the symmetrized split-step Fourier method (SSSFM) is widely used to improve the accuracy as in [34,37]: $A(z+\Delta z,T) = \exp\langle\frac{\Delta z}{2}\widehat{D}(\omega)\rangle \cdot \exp\langle\int_z^{z+\Delta z}\widehat{N}(z',T)dz'\rangle \cdot \exp\langle\frac{\Delta z}{2}\widehat{D}(\omega)\rangle A(z,T)$, which, however, can only treat the conventional case, i.e., there are only frequency-dependent dispersion operators and time-dependent nonlinear operators without $\widehat{G}(\omega,T)$. Hereafter, we take GPM into account and derive a SSSFM form for the GPC-NLSE:

$$\begin{aligned} A(z+\Delta z,T) = \exp\left\langle\frac{\Delta z}{4}\widehat{D}(\omega)\right\rangle \cdot \exp\left\langle\int_z^{z+\frac{\Delta z}{2}}\widehat{N}(z',T)dz'\right\rangle \cdot \exp\left\langle\frac{\Delta z}{4}\widehat{D}(\omega)\right\rangle \cdot \exp\left\langle\int_z^{z+\Delta z}\widehat{G}(z',\omega,T)dz'\right\rangle \\ \cdot \exp\left\langle\frac{\Delta z}{4}\widehat{D}(\omega)\right\rangle \cdot \exp\left\langle\int_{z+\frac{\Delta z}{2}}^{z+\Delta z}\widehat{N}(z',T)dz'\right\rangle \cdot \exp\left\langle\frac{\Delta z}{4}\widehat{D}(\omega)\right\rangle A(z,T). \end{aligned} \quad (17)$$

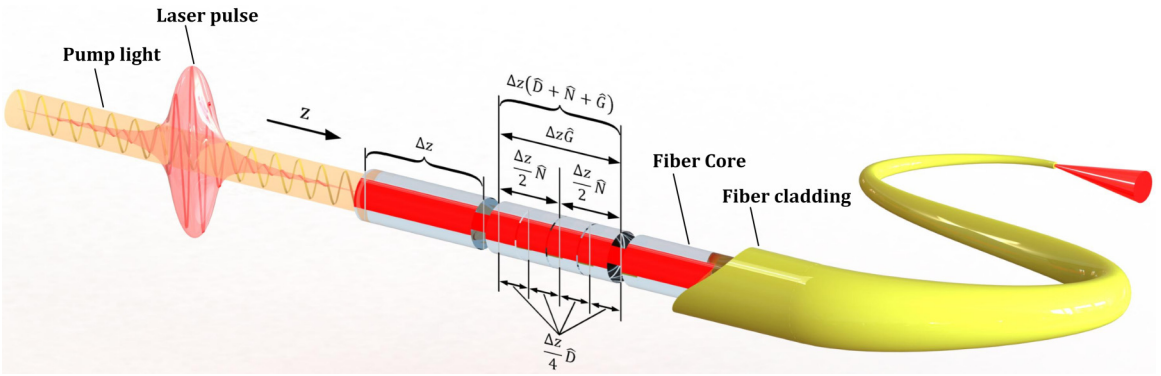

FIG. 2. Schematic illustration of the numerical simulation for GPC-NLSE using the SSSFM form. The fiber length is divided into a large number of segments with length Δz. Within a segment, the gain of the chirped laser pulse under continuous-wave pump light is assumed to be lumped at the midplane and the nonlinearity is lumped at the 1/4 and 3/4 segment length planes.

The accuracy of the SSSFM method can be further improved by evaluating the integral in Eq. (17) more accurately using various numerical methods. In this work, the trapezoidal rule is employed to approximate the integral by $\int_z^{z+\Delta z} \widehat{X}(z')dz' \approx \frac{\Delta z}{2}[\widehat{X}(z) + \widehat{X}(z+\Delta z)]$. Therefore, it is necessary to use an iterative procedure in the numerical model to replace $\widehat{X}(z+\Delta z)$ by $\widehat{X}(z)$, where $\widehat{X}$ represents $\widehat{D}$, $\widehat{N}$, and $\widehat{G}$. Equation (17) is used to estimate $A(z+\Delta z)$, which in turn is used to calculate the new value of $\widehat{X}(z+\Delta z)$. A more accurate $A(z+\Delta z)$ can then be obtained by performing a more accurate numerical integration of $\int_z^{z+\Delta z} \widehat{X}(z')dz'$.

The implementation of our new form of the SSSFM is illustrated in Fig. 2. The fiber length is divided into a large number of segments and the optical pulse travels from segment to segment as prescribed by Eq. (17). The procedure can be put in a more specific way as follows: (1) we consider the dispersion and nonlinearity in the first half-segment length $\Delta z/2$, in which the optical field $A(z,T)$ first propagates for a distance $\Delta z/4$ with only a frequency-dependent dispersion term using the FFT algorithm, and then the field is multiplied by a nonlinear term that represents the effect of nonlinearity over this segment length $\Delta z/2$ at position $z+\Delta z/4$, and finally the field propagates for the next distance $\Delta z/4$ with dispersion only; (2) at the midplane $z+\Delta z/2$, the field is multiplied by the gain term via Eq. (16) that represents the frequency-time-dependent gain effect over the whole segment length Δz; (3) the field propagates the remaining distance $\Delta z/2$ with dispersion and nonlinearity as the processes in step (1), and the nonlinearity is revealed at $z+3\Delta z/4$. Although the SSSFM procedure is time consuming, it can still reduce the overall computing time if the step size Δz can be increased owing to the improved accuracy of the numerical algorithm.

III. EXPERIMENTAL SETUP

A series of experiments have been performed to study the GPM effect in the YDF CPA system. The experimental setup is illustrated in Fig. 3. All the fibers used in this experiment were single mode. The front end was an all-normal-dispersion nonlinear amplifying loop mirror-mode-locked laser [38]. The output laser was 50:1 split by an output coupler, and the 2% portion of the signal was used as a trigger source for the oscilloscope. At monitor 1, the average power of the seed was about $P_{\text{ave}}|_{z=0} = 20$ mW and the repetition rate $f_r = 8$ MHz. The duration of the seed pulse was about 30 ps FWHM with a corresponding Fourier transform limit pulse width of about 200 fs. Then the seed chirped pulse was positively stretched to about $\tau_0 = 1.2$ ns by a stretcher, including a circulator and a chirped Bragg fiber grating. Therefore, according to Agrawal's criterion [34] that $\tau_0 > 5$ ps and $(\omega_0\tau_0)^{-1} < 0.001$, the self-steepening and Raman effects are negligible in our CPA process. After stretching, the wave form and spectrum were recorded at monitor 2, as shown in Figs. 4(a) and 4(b). As can be seen, the seed-pulse wave form before CPA has a self-steepening aberrant profile, the spectrum of which has two very steep edges. For the CPA system, the stretched pulses were amplified in the SM-YDF with a length of $L = 1.2$ m and an absorption coefficient of $\alpha = 250$ dB/m, being forwardly pumped by the laser diode (LD). The YDF ion-doping concentration relates to the absorption by $N_{\text{tot}} = \alpha/[10\sigma_{\text{ab}}^{(\text{p})}\Gamma_{\text{p}} \lg e]$. A short-length and large-absorption YDF was selected as the active medium to decrease the dispersion and nonlinearity in contrast to the gain. The 976-nm LD can provide the cw power up to 750 mW through the wavelength division multiplexers into the fiber core. In this experiment, the

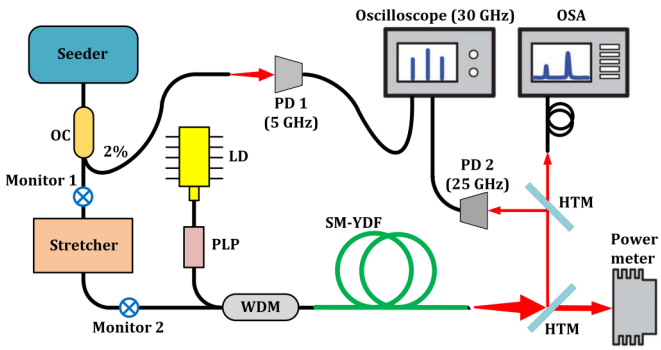

FIG. 3. Schematic of the experimental setup, the signals at monitor 1 and monitor 2 are also detected by PD 2. LD: laser diode, PLP: pump laser protector, WDM: wavelength division multiplexers, OC: output coupler, OSA: optical spectrum analyzer, HTM: high transmitting mirror, SM-YDF: single-mode Yb-doped fiber, PD: photon detector.

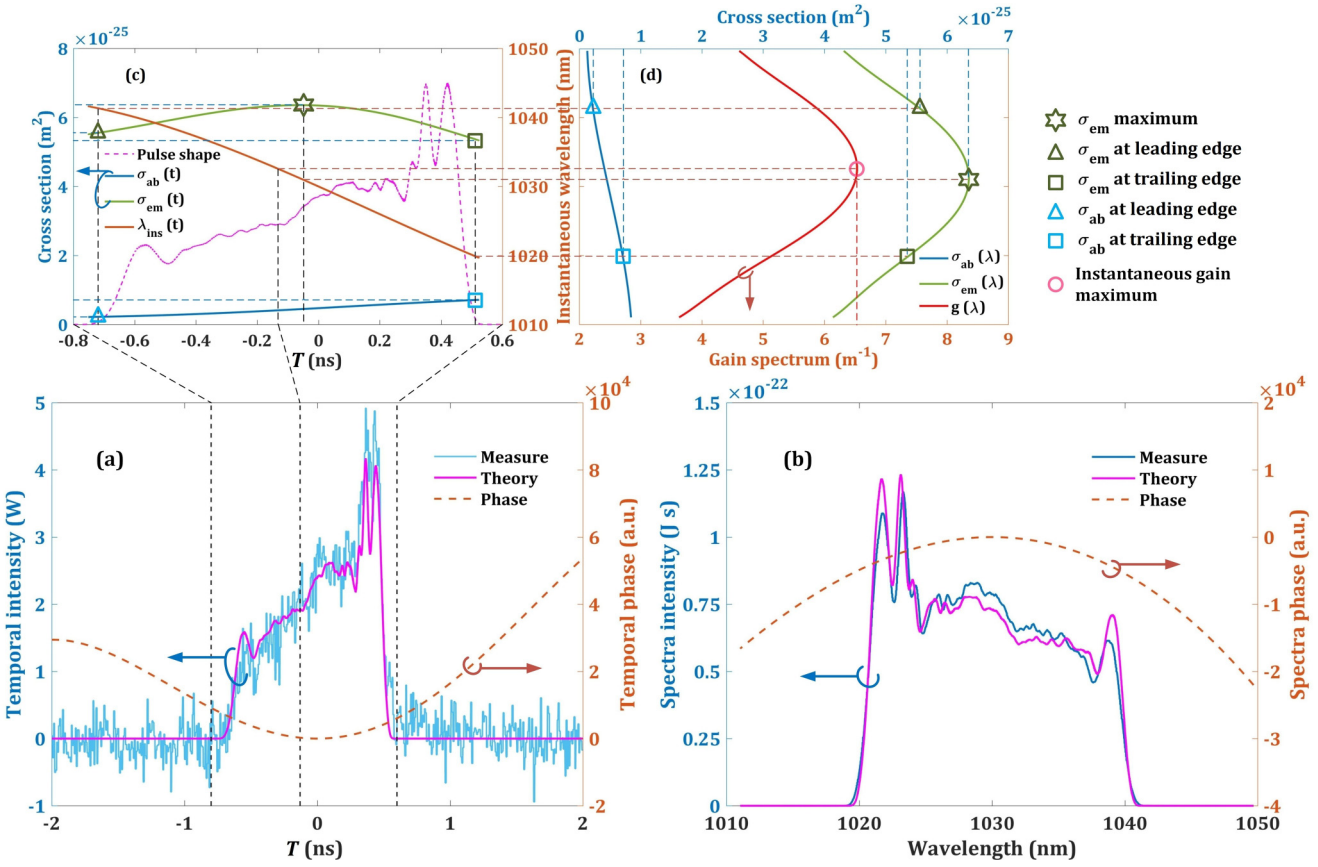

FIG. 4. (a) The temporal experimental and simulated intensities with phases, (b) the spectral experimental and simulated intensities of the seed pulse via CBIM. (c) An insert and scaling of (a), the instantaneous wavelength and the instantaneous induced temporal cross sections in the pulse region. (d) An insert of (c), the frequency-dependent cross sections and gain with their correlation to instantaneous wavelength.

LD provided $P_p^+|_{z=0} = 560$ mW for cw fiber core pumping. Other parameters used in this work are listed in Table I.

The pulse wave forms were measured by the combination of two high-speed photodetectors and a 30-GHz bandwidth sampling oscilloscope (Agilent 86100A-86106A) in which one of the photodetectors (Thorlabs DET025A/M, 2 GHz) was used to provide the output trigger for the oscilloscope, and the other photodetector (New Focus Model-1414, 25 GHz) was used to measure the wave forms. The pulse spectrum was measured by an optical spectrum analyzer (Yokogawa AQ6370) at a resolution of 0.1 nm. The laser power was measured by the thermopile power-meter head (Ophir PD300-1W).

TABLE I. Parameter settings used in this work.

Symbol	Value (Ref.)	Symbol	Value (Ref.)
c	2.998×10^{8} m/s	c_p	2.067×10^{8} m/s [33]
h	6.626×10^{-25} J s	c_s	2.067×10^{8} m/s [33]
λ_p	976 nm	α_p	5×10^{-3} m^{-1} [32]
λ_s (λ_0)	1030 nm	α_s	5×10^{-3} m^{-1} [32]
$\sigma_{ab}^{(p)}$	26.1×10^{-25} m^2 [39]	Γ_p	0.82 [32]
$\sigma_{ab}^{(s)}$	47.5×10^{-27} m^2 [39]	Γ_s	0.82 [32]
$\sigma_{em}^{(p)}$	25.8×10^{-25} m^2 [39]	n_2	2.6×10^{-20} m^2/W [34]
$\sigma_{em}^{(s)}$	6.0×10^{-25} m^2 [39]	γ	0.0047 W m^{-1} [12]
τ	840 μs [39]	β_2	24.2 ps^2/km [40]
a_c	6 μm	β_3	0.024 ps^2/km [40]

IV. RESULTS AND DISCUSSION

A. Initial seed gain and phase

In order to study the GPM effect in pulse evolution, the actual temporal and spectral intensities and phases must be obtained. The normalized functions of the temporal and spectral intensities were calculated, each of which was then multiplied by the value of pulse energy so that the integral of the obtained intensity is equal to the pulse energy. The theoretical pulse energy is calculated as $E_p = \int_{T_r/2}^{-T_r/2} |A(T)|^2 dT$, where $T_r = 1/f_r$ is the pulse repetition period. We also designed a chirp-coefficient bisection iteration method (CBIM) to solve the temporal and spectral phases based on the measured temporal and spectral intensities (see Appendix B). After several iterations, the solved temporal power $P_s(T)$ and spectral intensity $I_s(\omega)$ agree closely with the measured data. Then, we can obtain the $P_s(T)$ and $I_s(\omega)$ as the theoretical temporal and spectral intensities, $\phi(T)$ and $\varphi(\omega)$ as the theoretical temporal and spectral phase functions, and $A(T) = \sqrt{P_s(T)}e^{i\phi(T)}$ and $\tilde{E}(\omega) = \sqrt{I_s(\omega)}e^{i\varphi(\omega)}$ as the theoretical complex envelope and complex spectrum. The experimental temporal power and spectral intensity are shown as the blue (light gray) solid lines in Figs. 4(a) and 4(b). The

simulated temporal and spectral intensities are shown as the purple (dark gray) solid lines, and phases are shown as the red dashed lines in Figs. 4(a) and 4(b). All simulated results of the CBIM agree well with the measured results.

As the temporal and spectral intensities with phase distributions of the stretched seed pulse are all obtained, the initial conditions are sufficient for solving the GPC-NLSE. From the theoretical temporal chirped phase $\phi(T)$, the chirped instantaneous wavelength $\lambda_{\rm ins}(T) = 2\pi c/\omega_{\rm ins}(T)$ was obtained [Fig. 4(c); red (middle) solid line]. The chirped instantaneous frequency is redshifted (a shift toward longer wavelengths) at the pulse leading edge and blueshifted (a shift toward shorter wavelengths) at the pulse trailing edge; this agrees with the general principle regarding a positively stretched chirped pulse. According to the frequency-dependent absorption and emission cross sections [Fig. 4(d); blue (left) and green (right) solid lines], the temporal cross section changes induced by the instantaneous frequency, corresponding to $\sigma_{\rm ab}[\omega_{\rm ins}(T)]$ and $\sigma_{\rm em}[\omega_{\rm ins}(T)]$, were plotted [Fig. 4(c); blue (lower) and green (upper) solid lines]. The population densities were then obtained by solving the rate equations (see Appendix C for details), from which the frequency-time-dependent gain operator was obtained via Eqs. (8), (9), and (14) from the instantaneous wavelength-induced temporal gain for an average population distribution [Fig. 4(d); red (middle) solid line]. As can be seen, the maximum temporal gain of about 6.6 $\rm m^{-1}$ occurs at about $T = -130$ ps. Thus, the GPC-NLSE can be used to solve the pulse propagating through the next segment.

B. Pulse evolution with GPM

From the solution of the rate equations, the spatial gain dispersion relationship Eq. (9) can be obtained [Fig. 5(a)]. With the spatiotemporal population distributions $N_1(z,T)$ and $N_2(z,T)$, the spatiotemporal gain Eq. (8) can be derived [Fig. 5(b)]. The chaotic behavior of the spatiotemporal gain profiles at two wings in Fig. 5(b) are futile where the intensity is zero. The values in the pulse region of about -0.8 ns $< T <$ 0.6 ns are actually effective. Then, the comprehensive spatial time- and wavelength-dependent gain Eq. (14) can be obtained. Figure 6 depicts this gain at $z = 0$, $z = 0.6$ m, and $z = 1.2$ m, in which the evolution of its profile along the path of propagation from the positive-gain to the laser-reabsorption region is evident. The gain profiles in the positive-gain region are essentially convex around the center of the retarded time and the center wavelength but flatten as the pulse propagates towards the saturation region.

The evolutions of the temporal and spectral intensities for the pulse during CPA [Figs. 7(a) and 7(c)] show that the intensities are growing in the positive-gain region and barely change in the saturation region. This is in accordance with the principle of average laser power evolution. The simulated output temporal and spectral intensities [Figs. 7(b) and 7(d); red (dark gray) solid lines] show good agreement with the corresponding measured intensities [Figs. 7(b) and 7(d); blue (light gray) solid lines]. The simulated output pulse energy is $E_{\rm p}|_{z=L} = \int_{-T_{\rm r}/2}^{T_{\rm r}/2} |A(L,T)|^2 dT = \int_{-\infty}^{\infty} |\widetilde{E}(L,\omega)|^2 d\omega = 60.72$ nJ, which agrees with the measured pulse energy 57.25 nJ within acceptable error tolerance.

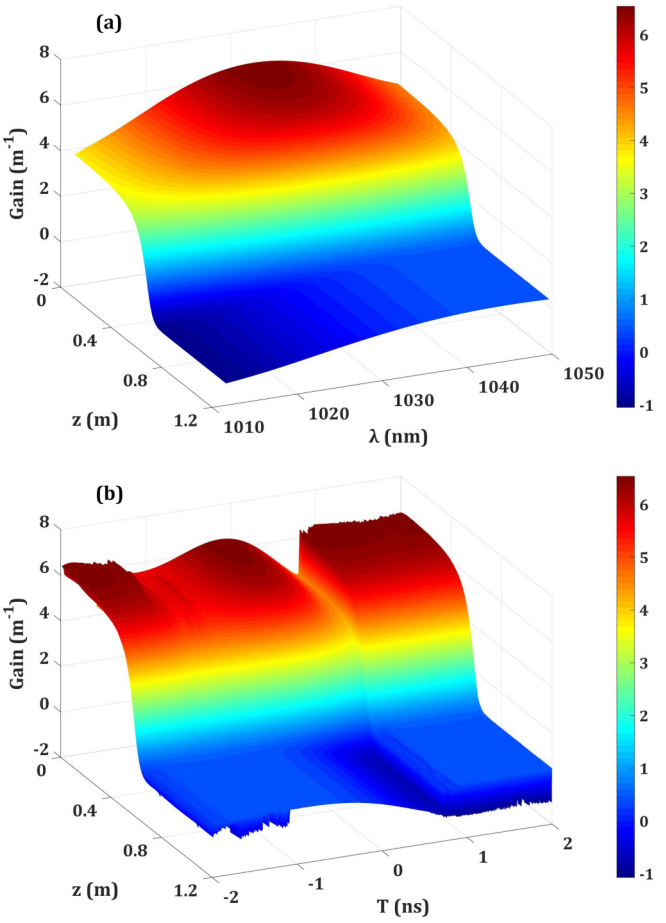

FIG. 5. The spatial (a) gain dispersion relationship $g_\omega(z,\lambda)$ and (b) temporal gain relationship $g_t(z,t)$ in the YDF CPA.

C. Output results and self-steepening compensation via GPM

The seed pulse has an obvious self-steepening temporal shape, with a smoother profile around the pulse leading edge as well as a profile with sharp oscillation around the pulse trailing edge [Fig. 4(a)], the shape of which is unwanted for mode-locked laser pulses. However, focusing on the

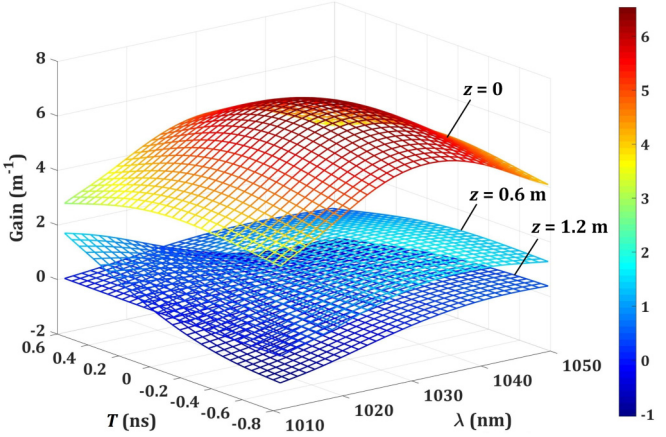

FIG. 6. The time- and wavelength-dependent gain $g(z,\lambda,T)$ at various propagating distances, $z = 0$, $z = 0.6$ m, and $z = 1.2$ m in the YDF CPA.

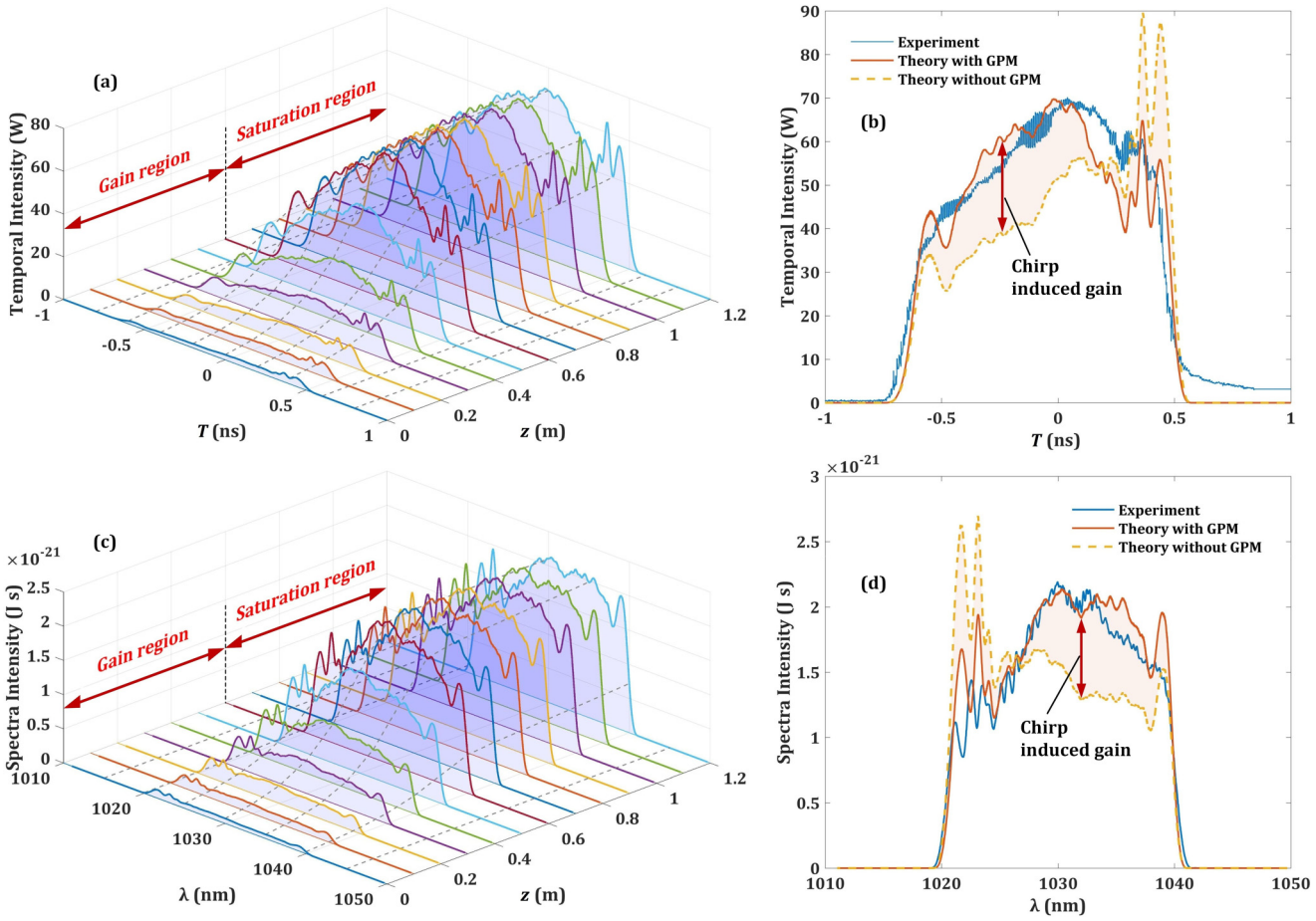

FIG. 7. (a) The evolution of the temporal intensities of the propagating pulse and (b) corresponding simulated and experimental output results; (c) the evolution of the spectra intensities of the propagating pulse and (d) corresponding simulated and experimental output results.

wave-form variations in Fig. 7(a), the serious self-steepening present in the seed pulse is appreciably compensated during the amplification. In contrast, the output spectrum has a better shape than the seed spectrum. The explanation is that the smoother region may have a larger instantaneous gain than the oscillatory edge owing to the convex profile of the comprehensive gain profiles induced by GPM.

A simulation without considering GPM effect was also performed, i.e., the instantaneous frequency-induced gain effect was neglected. The corresponding output temporal intensity and spectrum are marked as the orange dashed lines in Figs. 7(b) and 7(d), respectively. Although the simulated output pulse energy of 53.64 nJ is also close to the measured value, the wave form differs greatly as the measured shape and the self-steepening compensation phenomenon cannot be simulated in this case. Indeed, the difference between the results with and without GPM is indicative of the chirp-induced gain [Figs. 7(b) and 7(d); faint red (gray) area]. Therefore, it has been verified that the self-steepening can be compensated by the GPM effect.

V. CONCLUSION

In summary, the GPM effect in CPA is theoretically and experimentally demonstrated. In theory, the GPC-NLSE is proposed to characterize the GPM, in which the gain is accurately solved by the population dynamics involving the gain induced by the instantaneous chirped frequency. In the experiment, a short-length and high-gain YDF CPA system was established to scale a self-steepening aberrant seed pulse with an average power of 20 mW and the repetition rate of 8 MHz. After amplification, the output average power and pulse energy were 458.0 mW and 57.25 nJ, respectively, which are close to the corresponding simulated results of 490.3 mW and 60.72 nJ. The simulated wave forms and spectra show great agreement with the experimental results, in contrast to the model without GPM. Additionally, the self-steepening aberration of the seed pulse is automatically compensated in the output pulse after CPA. This compensation phenomenon is confirmed to be induced by the GPM effect. The GPC-NLSE and GPM theory can be further applied in fine pulse shaping, phase modulation, distortion compensation, etc., in various CPA systems.

ACKNOWLEDGMENT

This work is funded by the National Natural Science Foundation of China (NSFC) (Contract No. 61675114) and the Tsinghua University (THU) Initiative Scientific Research Program (Contract No. 20151080709).

APPENDIX A: CONVENTIONAL NLSE INCLUDING GAIN

Considering gain, the NLSE is always written as [5–13,15–17,34]

$$\frac{\partial A}{\partial z} = \underbrace{-\frac{i\beta_2}{2}\frac{\partial^2 A}{\partial T^2} + \frac{\beta_3}{6}\frac{\partial^3 A}{\partial T^3}}_{\text{dispersion}} + \underbrace{i\gamma|A|^2 A}_{\text{Kerr effect}} + \underbrace{\frac{g}{2}A + \frac{g}{2\Omega^2}\frac{\partial^2 A}{\partial T^2}}_{\text{gain}}, \tag{A1}$$

where the gain saturation relations, $g = g_0 \exp(-E_p/E_{sat})$ [11,15,17], $g = g_0/(1 + E_p/E_{sat})$ [12,13], and the temporal relation $g = g_0/(1 + |A|^2/P_{sat})$ [16] are always used to characterize the gain saturation effect. Here $E_p = \int |A|^2 dT$, E_{sat} (P_{sat}) is the saturation energy (power), and g_0 is the small signal gain. Unfortunately, these relations are only applicable to the steady state and the accurate temporal gain must be solved by the rate equations [18,30]. For the frequency-dependent relationship, a Gaussian or its approximate parabolic profile $g(\omega) = g_0 \exp(-\tilde{\omega}^2/\Omega^2) \approx g_0(1 - \tilde{\omega}^2/\Omega^2)$ [8–11,15–17] is widely used, where $\tilde{\omega} = \omega - \omega_0$ and $\omega = 2\pi c/\lambda$. Therefore, the operator $(1 + \Omega^{-2}\partial^2/\partial T^2)$ in Eq. (A1) represents the frequency-dependent principle based on the Fourier transform relationship. However, the actual gain spectrum of the active medium is not always a simple Gaussian distribution, so that the conventional NLSE can only roughly describe the light field evolution but cannot solve the fine structure of the pulse and spectrum. The Raman and self-steepening terms are omitted because these effects are very weak during the CPA in this work.

APPENDIX B: CHIRP BISECTION ITERATION METHOD

The nonlinear chirped temporal or spectral phase are expressed as a quartic polynomial:

$$\phi(T) = C_{t1}T^2 + C_{t2}T^3 + C_{t3}T^4, \tag{B1}$$

$$\varphi(\omega) = C_{\omega 1}\tilde{\omega}^2 + C_{\omega 2}\tilde{\omega}^3 + C_{\omega 3}\tilde{\omega}^4, \tag{B2}$$

where C_{t1}, C_{t2}, and C_{t3} are temporal linear, second-order, and third-order chirp coefficients, respectively, and $C_{\omega 1}$, $C_{\omega 2}$, and $C_{\omega 3}$ are spectral linear, second-order, and third-order chirp coefficients, respectively. The chirps of order higher than 3 are omitted. Therefore, the temporal and spectral light fields are given by

$$E(T) = \sqrt{P_s(T)}e^{[i(\omega_0 T + C_{t1}T^2 + C_{t2}T^3 + C_{t3}T^4) + \cdots]}, \tag{B3}$$

$$\tilde{E}(\omega) = \sqrt{I_s(\omega)}e^{[i(C_{\omega 1}\tilde{\omega}^2 + C_{\omega 2}\tilde{\omega}^3 + C_{\omega 3}\tilde{\omega}^4) + \cdots]}, \tag{B4}$$

obeying the Fourier transform relations

$$E(T) = \mathcal{F}^{-1}[\tilde{E}(\omega)] = \frac{1}{\sqrt{2\pi}}\int_{-\infty}^{\infty} \tilde{E}(\omega)e^{i\omega T}d\omega, \tag{B5}$$

$$\tilde{E}(\omega) = \mathcal{F}[E(T)] = \frac{1}{\sqrt{2\pi}}\int_{-\infty}^{\infty} E(T)e^{-i\omega T}dT. \tag{B6}$$

The temporal and spectral chirp coefficients of various orders, $C_{tn}, C_{\omega n}, n = 1,2,3,\ldots,N$ (N represents the cutoff order), are determined one-by-one by the following procedure:

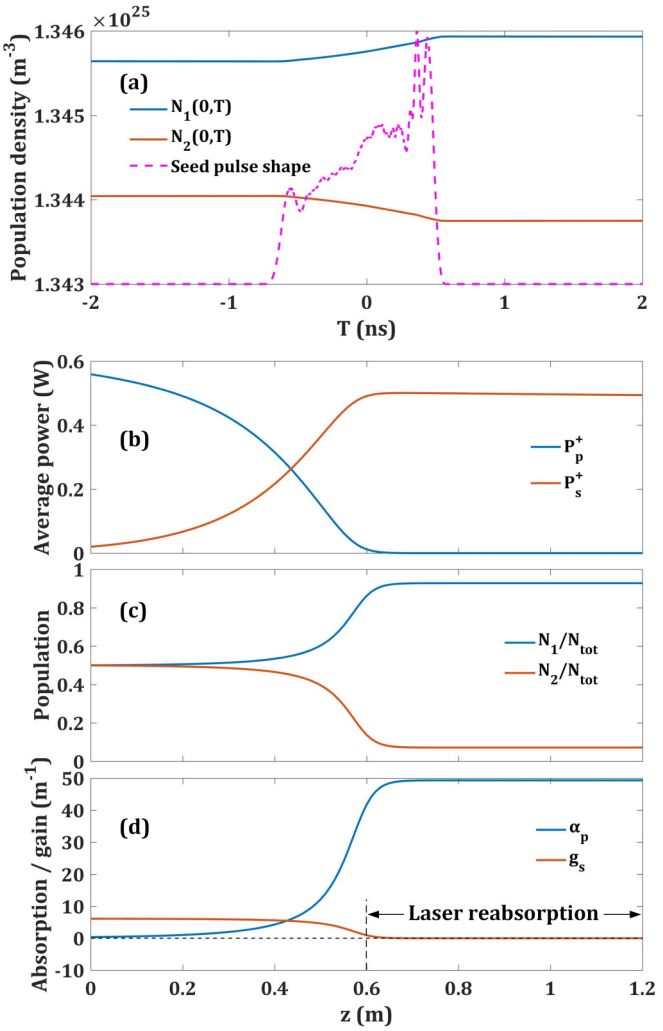

FIG. 8. (a) The temporal upper- and lower-state population densities in pulse range at $z = 0$. The average (b) laser and pump powers, (c) upper- and lower-state population, and (d) pump absorption and laser gain along the propagating distance.

Step 1: (Predetermine first-order chirp coefficients). First, make an upper estimate and lower estimate of the first-order spectral chirp coefficients, $C_{\omega 1}^{(1)}$ and $C_{\omega 1}^{(2)}$, and set higher-order chirp coefficients as zero. The actual first-order spectral chirp coefficient should be in the range $[C_{\omega 1}^{(1)}, C_{\omega 1}^{(2)}]$. Then, substitute them into the field function Eq. (B4) and perform the inverse Fourier transform Eq. (B5) to obtain the functions $F_t^{(1)}$ and $F_t^{(2)}$. Next, compute the standard deviations $D_1 = \mathrm{Std}(|F_t^{(1)}|^2, P_s)$ and $D_2 = \mathrm{Std}(|F_t^{(2)}|^2, P_s)$. A smaller deviation value denotes better accordance, and the bisection method can then be applied to further narrow the range of the first-order chirp coefficients, i.e., if $D_1 > D_2$, the next search range should be $[(C_{\omega 1}^{(1)} + C_{\omega 1}^{(2)})/2, C_{\omega 1}^{(2)}]$. After gradually narrowing the search range within a tolerance range, the first-order spectral chirp coefficient is ultimately determined.

The temporal first-order chirp coefficient is determined similarly using Eqs. (B3) and (B6).

Step 2: (Predetermine nth-order chirp coefficient). First, with the predetermined lower-order chirp coefficients fixed, make an upper estimate and lower estimate of the nth-order

spectral chirp coefficient of $C_{\omega n}^{(1)}$ and $C_{\omega n}^{(2)}$, and set higher-order chirp coefficients as zero. The actual nth-order spectral chirp coefficient should be in the range $[C_{\omega n}^{(1)}, C_{\omega n}^{(2)}]$. Then, substitute them into the field function Eq. (B4) and perform the inverse Fourier transform Eq. (B5) to obtain the functions $F_t^{(1)}$ and $F_t^{(2)}$. Next, compute the standard deviations $D_1 = \mathrm{Std}(|F_t^{(1)}|^2, P_s)$ and $D_2 = \mathrm{Std}(|F_t^{(2)}|^2, P_s)$. As before, with a smaller deviation value indicating a better agreement, the bisection method can be applied to further narrow the range of the nth-order chirp coefficient, i.e., if $D_1 > D_2$, the next search range should be $[(C_{\omega n}^{(1)} + C_{\omega n}^{(2)})/2, C_{\omega n}^{(2)}]$. After gradually narrowing the search range within a tolerance range, the nth-order spectral chirp coefficient is ultimately determined. The temporal nth-order chirp coefficient is determined similarly using Eqs. (B3) and (B6).

The above two steps can already determine the chirp coefficients of various orders. However, the influence of higher-order chirps is ignored when solving lower-order chirps. Thus, the following step 3 is necessary to modify the whole method.

Step 3: (Final determination of the chirp coefficients). A comprehensive external iteration algorithm is conducted by taking all investigated orders of chirp coefficients together to accommodate the interplay with all considered chirp orders present. The method involves first fixing the predetermined $n+1, n+2, \ldots, N$th-order chirp coefficients and then refresh the values of the nth-order chirp coefficients. After several iterations, the various chirp coefficients will converge to a stable solution. When the error converges to within tolerance range, the chirp coefficients of various orders are refreshed and finally determined.

With the various chirp coefficients evaluated, the temporal and spectral light fields with full amplitude and phase information can be obtained.

APPENDIX C: SOLUTION OF RATE EQUATIONS

In the rate equations, Eqs. (1)–(3), the effective absorption and emission cross sections are calculated using [31]

$$\sigma_{\mathrm{ab}}^{(\mathrm{m})} = \frac{\int_{-\infty}^{\infty} I_{\mathrm{m}}(\lambda - \lambda_{\mathrm{m}})\sigma_{\mathrm{ab}}(\lambda - \lambda_{\mathrm{m}})d\lambda}{\int_{-\infty}^{\infty} I_{\mathrm{m}}(\lambda - \lambda_{\mathrm{m}})d\lambda}, \tag{C1}$$

$$\sigma_{\mathrm{em}}^{(\mathrm{m})} = \frac{\int_{-\infty}^{\infty} I_{\mathrm{m}}(\lambda - \lambda_{\mathrm{m}})\sigma_{\mathrm{em}}(\lambda - \lambda_{\mathrm{m}})d\lambda}{\int_{-\infty}^{\infty} I_{\mathrm{m}}(\lambda - \lambda_{\mathrm{m}})d\lambda}, \tag{C2}$$

where "m" represents "s" or "p."

Because the pulse sequence has a rather high repetition rate of 8 MHz compared with the response rate of YDF ($f_r \gg 3/\tau \approx 3.6$ kHz) [18], the spatial average power distribution should have nearly no difference from that of the cw seed with identical initial average power. Under the conditions of a cw pumped stable output pulse train, the temporal changes of the upper- and lower-state population densities in the first segment are solved by the rate equations, Eqs. (1)–(3), as shown in Fig. 8(a). In this work, the pump and laser are both forward single-pass in the YDF amplifier, and hence the powers of the backward direction are set to zero. Combined with the GPC-NLSE, various pulse parameters in the next segment can be solved, and then the pulse evolutions along the whole propagating distance are solved. The numerical results of the laser and pump average powers, the upper- and lower-state population, and the pump absorption and laser gain evolutions are shown in Figs. 8(b)–8(d). The maximum laser power takes place at about $z = 0.6$ m as a consequence of the laser-reabsorption effect.

[1] M. Gedalin, T. C. Scott, and Y. B. Band, Phys. Rev. Lett. **78**, 448 (1997).
[2] M. Trippenbach and Y. B. Band, Phys. Rev. A **56**, 4242 (1997).
[3] M. Trippenbach and Y. B. Band, Phys. Rev. A **57**, 4791 (1998).
[4] W. H. Renninger and F. W. Wise, Optica **1**, 101 (2014).
[5] L. H. Yin and G. P. Agrawal, Opt. Lett. **32**, 2031 (2007).
[6] N. C. Panoiu, X. P. Liu, and J. R. M. Osgood, Opt. Lett. **34**, 947 (2009).
[7] A. Blanco-Redondo, D. Eades, J. T. Li, S. Lefrancois, B. J. E. T. F. Krauss, and C. Husko, Optica **1**, 299 (2014).
[8] G. P. Agrawal, Opt. Lett. **16**, 226 (1991).
[9] G. P. Agrawal, IEEE J. Quantum Electron. **27**, 1843 (1991).
[10] I. Koltchanov, S. Kindt, K. Petermann, S. Diez, R. Ludwig, R. Schnabel, and H. G. Weber, IEEE J. Quantum Electron. **32**, 712 (1996).
[11] L. M. Zhao, C. Lu, H. Y. Tam, P. K. A. Wai, and D. Y. Tang, Appl. Opt. **48**, 5131 (2009).
[12] A. Chong, W. H. Renninger, and F. W. Wise, J. Opt. Soc. Am. B **25**, 140 (2008).
[13] W. H. Renninger, A. Chong, and F. W. Wise, Phys. Rev. A **82**, 021805 (2010).
[14] R. Paschotta, Opt. Express **25**, 19112 (2017).
[15] X. M. Liu, Phys. Rev. A **81**, 053819 (2010).
[16] T. Yoshida, H. Okunishi, K. Kyomoto, K. Kato, K. Shimabayashi, S. Inayoshi, M. Morioka, and S. Kawato, Appl. Sci. **5**, 1431 (2015).
[17] Y. Du and X. Shu, J. Opt. Soc. Am. B **34**, 553 (2017).
[18] A. Ozawa, T. Udem, U. D. Zeitner, T. W. Hansch, and P. Hommelhoff, Phys. Rev. A **82**, 033815 (2010).
[19] J. C. Delagnes and M. A. Bouchene, Phys. Rev. A **76**, 023422 (2007).
[20] M. D. Perry, F. G. Patterson, and J. Weston, Opt. Lett. **15**, 381 (1990).
[21] D. N. Schimpf, J. Limpert, and A. Tünnermann, Opt. Express **15**, 16945 (2007).
[22] C. L. Blanc, P. Curley, and F. Salin, Opt. Commun. **131**, 391 (1996).
[23] D. N. Papadopoulos, M. Hanna, F. Druon, and P. Georges, IEEE J. Quantum Electron. **15**, 182 (2009).
[24] P. Raybaut, F. Balembois, F. Druon, and P. Georges, IEEE J. Quantum Electron. **41**, 415 (2005).
[25] L. M. Frantz and J. S. Nodvik, J. Appl. Phys. **34**, 2346 (1963).

[26] W. H. Lowdermilk and J. E. Murray, J. Appl. Phys. **51**, 2436 (1980).
[27] L. Kuzneysova, F. W. Wise, S. Kane, and J. Squier, Appl. Phys. B **88**, 515 (2007).
[28] C. Pflaum, R. Hartmann, and Z. Rahimi, Proc. SPIE **9726**, 972610 (2015).
[29] J. S. Feehan, F. Ö. Ilday, W. S. Brocklesby, and J. H. V. Price, J. Opt. Soc. Am. B **33**, 1668 (2016).
[30] M. Eichhorn, Appl. Phys. B **93**, 269 (2008).
[31] E. Ji, Y. Shen, M. Nie, X. Fu, and Q. Liu, Appl. Phys. B **123**, 129 (2017).
[32] I. Kelson and A. A. Hardy, IEEE J. Quantum Electron. **34**, 1570 (1998).
[33] D. N. Schimpf, C. Ruchert, D. Nodop, J. Limpert, A. Tünnermann, and F. Salin, Opt. Express **16**, 17637 (2008).
[34] G. P. Agrawal, *Nonlinear Fiber Optics*, 4th ed. (Elsevier, New York, 2007).
[35] R. A. Fisher and W. K. Bischel, J. Appl. Phys. **46**, 4921 (1975).
[36] R. A. Fisher and W. K. Bischel, J. Math. Phys. **3**, 771 (1962).
[37] J. A. Fleck, Jr., J. R. Morris, and M. D. Feit, Appl. Phys. **10**, 129 (1976).
[38] G. Gao, H. Zhang, Y. Li, and D. Deng, Laser Phys. Lett. (to be published).
[39] R. Paschotta, J. Nilsson, A. C. Tropper, and D. C. Hanna, IEEE J. Quantum Electron. **33**, 1049 (1997).
[40] D. Mortag, T. Theeg, K. Hausmann, L. Grüner-Nielsen, K. G. Jespersen, U. Morgner, D. Wandt, D. Kracht, and J. Neumann, Opt. Commun. **285**, 706 (2012).